Precipitation and Cr depletion profiles of Inconel 182 during heat treatments and laser surface melting

Gang Bao[a,b], Motomichi Yamamoto[a], Kenji Shinozaki[a]*,

[a] Dept. of Mechanical System Engineering, Hiroshima University,

1-4-1 Higashi-Hiroshima, Hiroshima, Japan

[b] Babcock-Hitachi K.K., 3-36 Takara-machi, Kure, Hiroshima, Japan

* Corresponding author. Tel.: +81-82-424-7570; Fax: +81-82-424-7570; E-mail:

kshino@hiroshima-u.ac.jp

Precipitation and Cr depletion profiles of Inconel 182 during heat treatments and laser surface melting

Abstract

Thermodynamic and kinetic modeling was conducted to simulate Cr depletion profiles near grain boundaries in Inconel 182 during heat treatments and laser surface melting (LSM) using Thermo-Calc and DICTRA code. The effect of Nb addition was also considered in the modeling. Based on the good agreement with Cr concentration distributions during the heat treatments measured experimentally, Cr depletion profiles adjacent to grain boundaries during the heat treatments and the LSM process were modeled. The Cr depletion profiles were evaluated using the Cr depletion area below the critical Cr concentration for IGC/IGSCC (Intergranular Cracking/Intergranular Stress Corrosion Cracking) susceptibility (12 mass%). Compared with the result of the Streicher test, the calculated Cr depletion areas showed good agreement with IGC/IGSCC susceptibilities. The sample after stress relief (SR) treatment had the largest Cr depletion area and showed the poorest IGC/IGSCC resistance. Cr depletion showed some recovery during subsequent low temperature sensitization (LTS). The sample after the LSM process had the smallest Cr depletion area and showed the best IGC/IGSCC resistance.

Key words: Cr depletion, IGC/IGSCC susceptibility, Inconel 182, LSM, precipitation

1. Introduction

The nickel-based superalloy, Inconel 182 has been extensively used as a weld metal in light-water-reactor structural components in nuclear power plants in the past few

decades. The intergranular cracking/intergranular stress corrosion cracking (IGC/IGSCC) of Inconel 182 weld metal has been a major concern in the management and prediction of plant life. Some investigations have also reported that Inconel 182 is susceptible to IGC/IGSCC in higher temperature water and other caustic environments [1-6]. Recently, laser surface melting (LSM) has been considered as one of the useful surface modification techniques to repair and improve corrosion resistance of overlaying of Inconel 182 in parts of nuclear plants [7-9].

Grain boundary chemistry and microstructure have been recognized as the main factors affecting the IGC/IGSCC susceptibility of nickel-based superalloys. Commonly, the precipitation of Cr-rich carbides and the resultant creation of Cr depleted zones near grain boundaries have been known to play an important role in determining the alloy's susceptibility to IGC/IGSCC. Many studies have been performed to investigate the microstructural evolution of Inconel 182 weld metal during heat treatments as well as the resultant Cr depletion profiles [4-8, 10]. However, few have modeled the precipitation process and depletion profiles of Inconel 182.

In the present work, we establish a model to simulate the Cr depletion profile of Inconel 182 for the heat treatments and the LSM process using the Thermo-Calc and DICTRA code. This model is based on conventional diffusion equations solved by numerical methods. Experimental data from the literature have been collected to verify the simulation results. First, the model was proved by comparison with the experimental data; the calculations were then extended to cover wider temperature ranges and time durations. Finally, the IGC/IGSCC susceptibilities of Inconel 182 during the heat

treatments and the LSM process were evaluated and compared with the depletion parameters.

2. Material used and experimental procedures

2.1 Material used and specimen preparation

Table 1 shows the chemical composition of Inconel 182. The thermal cycle flow used is shown in Fig. 1. For Inconel 182, **shielded metal-arc welding** (SMAW) was used to clad the deposited metal. Then stress relief (SR) (898 K×86.4 ks) was performed to reduce the residual stress after the SMAW process. These two stages were used to simulate the weld metal of multi-pass welding. Low temperature sensitization (LTS) (773 K×86.4 ks) was performed to simulate the sensitization process after long-term operation. The LSM process was carried out on the specimen surface; finally the LTS treatment was performed again to verify the corrosion resistance of the material after the LSM process.

A Nd:YAG laser with 2 kW peak power was used for the LSM process. Ar was used as the shielding gas to prevent oxidation of the melted region. The LSM parameters used in the present study are shown in Table 2.

2.2 Corrosion test

The IGC/IGSCC susceptibility was evaluated in a solution of 400 ml H_2O, 233 ml H_2SO_4 and 50 g $Fe_2(SO_4)_3$ with the Streicher test. The specimens were cut into small samples of length 40 mm, width 8 mm and thickness 5 mm, and immersed in boiling solution for 86.4 ks. Then the samples were bent to reveal the IGC/IGSCC for observation. After the Streicher test, the maximum IGC depth in two cross sections was

measured by optical microscopy (OM) to evaluate the IGC/IGSCC susceptibility of Inconel 182.

2.3 Microstructure observation

The overall microstructure of the specimen was observed after electrolytic etching in 10% acetic acid solution under 10 V for 90 s. For the observation of carbides, the specimen of Inconel 182 was electrolytically etched in 85% orthophosphoric acid solution under 10 V for 20 s. Then the etched microstructure was examined separately using both optical microscopy (OM) and scanning electron microscopy (SEM). In order to analyze the crystal structures of precipitates, transmission electron microscopy (TEM) with energy dispersive X-rays (EDX) was adopted to identify the phase of precipitate by means of the extraction replica method. The polished specimen was etched in a solution of aqua regia for 60 s before carbon coating, and the specimen preparation technique for the extraction replica method is described in detail elsewhere [11].

3. Microstructure Characteristics

3.1 Optical microstructure observation

Figure 2 shows the optical microstructures of the specimens before and after the LSM process. It was different from the microstructure of the base metal of Inconel 600 before the LSM process [12]. The specimens of Inconel 182 before the LSM process showed a similar solidification microstructure which formed during the SMAW process. On the other hand, after the LSM process, a more refined microstructure with cellular morphology was obtained due to the rapid heating and cooling rate of the LSM procedure.

3.2 Intergranular microconstituent precipitation

Since the intergranular microconstituents play a very important role in determining the IGC/IGSCC susceptibility of materials, the distributions of intergranular microconstituents after the different heat treatments and the LSM process were examined, as shown in Fig. 3. In the specimen with SMAW, SR and LTS, film-like microconstituents were found on grain boundaries.

As the heat treatments progressed, additional tiny microconstituents had nucleated and grown along the grain boundaries, so the average coverage of microconstituents on the grain boundaries increased gradually. As shown in Fig. 3 (a), for the specimen of SMAW, only discontinuous microconstituents were found along the grain boundaries. The specimen after the SR treatment showed a semi-continuous morphology of microconstituent distribution along the grain boundaries (shown in Fig. 3 (b)), while Figure 3 (c) indicates that the microconstituent distribution on the grain boundaries after the LTS treatment was nearly continuous.

Fig. 3(d) demonstrates the SEM microstructure in LSM zone shown in Fig. 2(b), no microconstituents were found on the grain boundaries after the LSM procedure. This result indicates that the pre-existing continuous microconstituents after the sensitized treatment (LTS) had been completely dissolved into the matrix due to the high energy density of the laser beam irradiation and did not have sufficient time to re-precipitate in the laser melted region because of the extremely rapid cooling rate of the LSM process. As shown in Fig. 3 (e), there were no obvious changes occurring in the LSM specimen following the LTS treatment, and few microconstituents were found

on the grain boundaries.

3.3 Identification of intergranular microconstituents by TEM

To identify the phase and crystal structure of the carbide formed before the LSM process, TEM was used with the extraction replica method in specimens taken before the LSM procedure. The granular tiny microconstituents were identified as $M_{23}C_6$ (as shown in Fig. 4). The tiny Cr-rich $M_{23}C_6$ should correspond to film-like intergranular microconstituents observed by SEM. The phases of Inconel 182 identified under the different heat treatment conditions also agreed with other researchers' experimental observations [4, 5, 10].

3.4 Interdendritic microconstituents

In the overlaying of Inconel 182 weld metal, primary and eutectic NbC also formed during solidification in the SMAW process. Figure 5 shows the interdendritic NbC distribution after the SMAW procedure. SEM examination at higher magnification revealed some NbC carbides with typical eutectic morphology, which implies that they formed at the terminal stage of the solidification procedure. As shown in Fig. 6, TEM identification of such phase also proved it was NbC (lattice constant a=4.41 nm).

4. Simulation Model

4.1 Thermodynamic and Kinetic Model

The following simplifying assumptions were used in our model. The simulation is based on local equilibrium at the moving phase interface, which means the compositions of both matrix and carbide adjacent to the phase interface comply with the thermodynamic equilibrium. The carbon is considered as the interstitial

diffusing species and the other elements are taken into account as the substitutional species. The carbide growth is controlled by the diffusion of the substitutional components. The rate of transformation is controlled only by the component transport near the interface, thus we treat the diffusion problem for the heat treatments and the LSM process as a one-dimensional case.

In a multicomponent system, the diffusion of species is controlled by the diffusion equation shown below.

$$\frac{\partial c_k}{\partial t} = \frac{\partial}{\partial x}\left(-J_k\right) \quad \textbf{(1)}$$

Where c_k and J_k is the concentration and the diffusive flux of component k respectively. And the flux of species J_k corresponds to the Fick-Onsager law (as shown in equation 2), which means the flux of species is the function of diffusion coefficient and concentration gradient.

$$J_k = -\sum_{j=1}^{n-1} D_{kj}^{n} \nabla_{cj} \quad \textbf{(2)}$$

Where n is the species number and species n is dependent; D_{kj}^{n} is the diffusion coefficient matrix, and ∇_{cj} is the concentration gradient for species j. The diffusion coefficient matrix D_{kj}^{n}, which is used for the simulations, is obtained by both kinetic and thermodynamic databases. The thermodynamic matrix is obtained by Thermo-Calc with Nickel database, which is based on the minimization of the total Gibbs free energies of the individual phases in the system and on the calculation of phase diagrams approach (CALPHAD). The diffusion data are taken from DITRA databank of MOB2. After setting up the initial

conditions for simulation (carbide and matrix compositions, temperature), the diffusion coefficient matrix varies during the simulation, which is determined by DICTRA according to the corresponding variation of compositions of matrix and temperature during the calculation. The diffusivities of various species in the carbides are still unknown, thus, the carbides are therefore treated as non-diffusion phases.

The precipitation process can commonly be divided into three stages: nucleation, growth and coarsening. The coarsening process needs requires a long time closed to the equilibrium conditions, so it is not considered in present study. And since the nucleation process is quite complex and difficult to be simulated, no attempt is made to account for the carbide nucleation or incubation time, the carbide is assumed to be nucleated instantaneously.

4.2 Consideration of NbC

Although MC carbide has not been reported to have a direct influence on the corrosion resistance of material, it can affect corrosion resistance indirectly by reducing the amount of carbon available for the precipitation of Cr carbides such as $M_{23}C_6$ or M_7C_3. Thus, the temperature and duration of the heat treatment determine the amount of MC carbides, the ratio of MC to $M_{23}C_6$ or M_7C_3, and the final stress corrosion cracking (SCC) resistance of the alloy. The function of Nb in the weld metal of nickel-based superalloy is to stabilize the carbon by the formation of NbC. Thus, the formation of Cr-rich carbides ($M_{23}C_6$ or M_7C_3) is avoided and the susceptibility to IGC/IGSCC can be lowered.

The temperature range for common **post-weld heat treatment** (PWHT) is usually between 673 and 973 K since NbC is a relatively stable phase and does not decompose at low temperatures, and Cr-rich carbides such as $M_{23}C_6$ or M_7C_3 may form faster than NbC from the solid state matrix during heat treatments at lower temperatures. Cerjak et al. [13] had calculated the evolution of precipitates of heat-resistant Cr-steel CB8 during welding, and their results also proved that NbC was virtually unaffected by the thermal cycle of welding. Thus, for simplification, we assume that the primary and eutectic NbC formed during the solidification of the SMAW procedure undergoes no change during the sequential heat treatments (SR and LTS) at lower temperatures. The C amount in NbC is removed from the alloy's composition, and is assumed not to affect the Cr-rich carbide precipitation later, which means that no secondary precipitation of NbC is taken into account.

4.3 Setting up the problem

Considering the intergranular precipitation observed above, the intergranular carbides commonly showed semi-continuous or continuous morphology. Thus, we assumed that the Cr-rich carbide precipitated uniformly on the grain boundaries. The carbide type was assumed to be $M_{23}C_6$ according to the results of TEM identification.

For the precipitation calculation, which is very complex and time consuming, it is therefore restricted to the alloy with **the following** four major components: Fe, C, Cr and Ni, which are the most important elements for $M_{23}C_6$ precipitation. And only two phases of matrix and carbide were considered.

In the present model, only the growth process is considered. Rather than considering

the growth of carbide from zero size, a finite size (3 nm) was assumed as the initial carbide size for calculation. The matrix size was assumed as 3 and 0.5 μm for the specimens before and after the LSM process, respectively. For model verification with the experimental data from the literature, compositions the same as those used in the literature were adopted. For the calculation, actual heat treatment conditions were used. Since the diffusion speed of atoms under low temperature becomes much slower, thus, diffusion below the LTS temperature was omitted for simplification.

To sum up, **the calculations are preformed in a single cell containing one region in one dimension, which contains matrix phase and $M_{23}C_6$ carbide.** The initial grid settings for the carbide and matrix are 20 and 2000, respectively, and then the grid variation is determined by DICTRA automatically to achieve convergence during the calculation. The initial compositions of the matrix and carbide are calculated by Thermo-Calc with Nickel database according to the corresponding temperature and alloy compositions. The diffusion coefficients and concentrations of all elements at the interface between matrix and carbide are determined simultaneously by DICTRA according to the corresponding variation of compositions of matrix and temperature during the calculation. **And in the calculation, the automatic time step control is used, the smallest time step to reflect the time scale of the initial stage of our problem simulated. After the calculation performed on each grid for every time-step, the equilibrium is calculated by Thermo-Calc and the new phase compositions are obtained. And then the matrix compositions vary and the diffusion equations are solved according to the new matrix compositions.**

5. Calculation Results and Discussion

5.1 Model verification

Experimental data from the literature [5] that measured the intergranular Cr concentration profiles in Inconel 182 were used for model verification. For modeling, the same chemical compositions of Inconel 182 were used as reported in the literature [5].

5.1.1 Influence of NbC amount on precipitation of Cr-rich carbide

Since the amount of primary or eutectic NbC formed during solidification was not mentioned [5], we therefore assumed that the amount of primary or eutectic NbC (as well as TiC, etc.) was in direct proportion to the content of Nb (or Ti) in the alloy composition. **According to the SEM observation and EDX analysis, NbC was identified,** the areal amount of NbC was measured from at least 10 SEM micrographs taken randomly, and we used the areal amount of NbC to approximate the volume amount.

Because atomic fraction is used in Thermo-Calc, we must transform the volume amount into the atomic amount. The molar volumes for the γ matrix and NbC have to be used. Since no data about the molar volume for the γ matrix and NbC could be obtained, we calculated them from their lattice structure according to the following **equation 3:**

$$V_{\text{molar}} = \frac{N_{\text{A}}}{x} \times a^3 \qquad \textbf{(3)}$$

where V_{molar} is the molar volume of microconstituents, N_{A} is Avogadro's number (6.022×10^{23}), x is the atomic number in one crystal lattice, and a is the lattice constant of the microconstituent. The lattice constants of γ matrix [14] and NbC are 0.3562 nm

and 0.4698 nm, respectively. Table 3 gives the calculated results of NbC amount after the SMAW process.

The atomic percent of NbC in Inconel 182 [5] is 0.12 at% (0.24 vol.%) which corresponds to the equilibrium volume fraction of NbC in the alloy at 1218 K calculated by Thermo-Calc. As mentioned above, we assume that the primary or eutectic NbC has no influence on the precipitation of Cr carbides during the procedure after solidification of the SMAW and the following heat treatments. Thus, we selected the chemical compositions of γ at 1218 K as the initial matrix compositions for Inconel 182 [5], which were determined by the calculation mentioned above. We only considered the Ni, Fe, Cr and C in the carbide precipitation procedure later.

5.1.2 Comparison of calculated results and experimental data

Because no SMAW parameters were mentioned in Ref. [5], so we assumed the same conditions of the SMAW process in our study, and the thermal cycle of SMAW is calculated by **equation 4**, which is described elsewhere [15].

$$T = T_0 + \frac{Q_{\mathrm{p}}}{2\pi k} \cdot \frac{1}{vt} \qquad \textbf{(4)}$$

where T_0 is room temperature, k is the thermal conductivity, v is the welding speed, t is time, and Q_{p} is the heat input which is calculated by **equation 5**, where η is the thermal efficiency, and E and I are the arc voltage and welding current, respectively. Table 4 gives the parameters used for the SMAW process.

$$Q_{\mathrm{p}} = 0.24\eta EI \qquad (5)$$

Since the SMAW procedure consists of melting and solidification procedures which are very complex and difficult to calculate by numerical simulation, and considering the

fact that precipitation of Cr carbide occurs during the cooling procedure after solidification, we assume that the precipitation of Cr-rich carbides usually occurs from the equilibrium precipitation temperature of $M_{23}C_6$ (calculated by Thermo-Calc with the initial composition of matrix) during the cooling procedure of the SMAW process. We omit the solute microsegregation which occurred during the solidification procedure of SMAW since this seems to have little effect on Cr depletion profiles according to an earlier study on Inconel 600 [12]. The lowest precipitation temperature of the SMAW process was selected as 723 K which is the same temperature as used in subsequent heat treatment. **And since the cooling rate of welding is very fast, the influence of reheating by the sequential pass can be omitted, which means that only the single pass welding is considered in the model. Table 5 gives the initial compositions of carbide and matrix for simulation [5] calculated by Thermo-Calc at 1015K (equilibrium precipitation temperature of $M_{23}C_6$ for this alloy).**

Experimental data for Cr concentration distribution from the literature [5] was used for model verification. Figure 7 shows the comparison of experimental measurements and results calculated with the current model. The Cr depletion zone after the SMAW procedure is quite narrow, and becomes much wider after heat treatment at 888 K for 36 ks. The Cr depletion profiles virtually do not change during the heat treatment at 723 K for 720 ks probably due to the lower temperature. In general, the current model correctly predicts the Cr depletion profiles.

5.2 Modeling of SMAW, SMAW+SR, SMAW+SR+LTS, LSM and LSM+LTS processes

5.2.1 Calculation of Cr concentration distribution near the intergranular carbide

Since the results of the experimental data from the literature and those calculated with the current model have shown good agreement, we had sufficient confidence to apply the current model for our practical conditions. Using the thermal cycle shown in Fig. 1, the Cr depletion profiles during the practical heat treatments and the LSM process were calculated.

We deal with the heat treatments before the LSM process just as with the model used for the verification mentioned above. For the LSM process, the thermal cycle calculated by the FEM model [8] was used for diffusion calculation. **In a similar way like SMAW process, only the single pass LSM process is taken into account without the consideration of reheat effect by sequential LSM process.** Just as with the SMAW procedure, the LSM process also induces melting and solidification procedures which are very complex and difficult to calculate by numerical simulation. We also make the assumption that the precipitation of Cr-rich carbide usually occurs from the equilibrium precipitation temperature of $M_{23}C_6$ (calculated by Thermo-Calc) during the cooling procedure of LSM, and no consideration was made for the microsegregation which occurred during the LSM process. Since almost no NbC was found in the laser melted zone (LMZ), thus, no consideration of NbC was made for the LSM process. And the lowest precipitation temperature of the LSM process was selected as 773 K which is the same as the LTS temperature we used.

The calculation results are shown in Fig. 8. For the specimens after the LSM process, the Cr depletion zone is very narrow, whereas the Cr depletion zone becomes very large after the SR treatment.

5.2.2 Evaluation of Cr depletion profiles

The depletion parameter is adopted to quantitatively characterize the amount of material surrounding a grain boundary that is depleted in Cr. Since the minimum Cr concentration near the grain boundary is very important for the IGC/IGSCC susceptibility of material and the Cr depletion zone must possess a minimum width for IGC/IGSCC occurrence, the depletion area [16] under some critical Cr concentration with consideration of both minimum Cr content and Cr depletion width was used to evaluate the Cr depletion of Inconel 182 with the different heat treatments and the LSM process (as shown in Fig. 9). It has been reported that Inconel 182 is susceptible to IGSCC/IGC when the grain boundary Cr level is below approximately 12 mass% [4]. Thus, in our study, the critical Cr concentration of the depletion area for Inconel 182 was assumed to be 12 mass%. The depletion area for the different heat treatments and the LSM process was calculated from the simulation results above, and the evaluation results are summarized in Fig. 10. According to the calculation results, the Cr depletion area becomes largest after the SR treatment, while it becomes smaller during the subsequent LTS treatment. On the other hand, the Cr depletion areas for the SMAW, LSM and LSM+LTS processes are quite small.

5.3 Discussion

Taking into account the effects of NbC, the Cr depletion profiles of Inconel 182 were calculated and the IGC/IGSCC resistance of Inconel 182 under the different heat treatments and LSM process could be predicted very well.

Since the complex influences of microstructural and metallurgical factors were not

included in the current modeling (carbide nucleation, dislocation, etc.), the composition of the matrix and the heat treatment or processing parameters (temperature and time duration) would be the most significant factors which determined the final Cr depletion profiles.

The SMAW and LSM processes show a small Cr depletion area due to the rapid cooling rate and short time duration during the sensitization temperature range. In particular, the LSM process shows the smallest Cr depletion area due to its extremely fast cooling rate during laser processing, although the C concentration in the matrix for the SMAW process is lower. The SR treatment results in the largest Cr depletion area, most likely due to the longest time duration at the sensitization temperature of the material. The Cr depletion area after LTS treatment is smaller than that after SR treatment. This implies the recovery of the Cr concentration in the Cr depletion zone near the Cr-rich carbide precipitates; the Cr depletion is reduced during the LTS process following the SR treatment.

These results agree with the IGC/IGSCC susceptibilities evaluated by the Streicher test (as shown in Fig. 10). Since the Streicher test is sensitive to the extent of the Cr depletion region, we can conclude that the depletion areas calculated and the IGC/IGSCC susceptibilities show good agreement. Heat treatment inducing larger Cr depletion areas always gives poor IGC/IGSCC susceptibility. The analysis and calculation above also demonstrate that, with the present model, it is possible to predict the Cr depletion as well as the corresponding IGC/IGSCC susceptibility of Inconel 182 for different heat treatment conditions.

6. Conclusions

1. The Cr depletion profiles of Inconel 182 during the heat treatments and the LSM process were simulated with a one-dimensional thermodynamic diffusion model using Thermo-Calc and DICTRA Code. The influence of Nb was considered by removing the amount of carbon consumed by NbC formation, which was measured by experimental observations. The Cr concentration distributions around the intergranular carbide precipitates for different heat treatments were calculated and compared with experimental EDX measurements from the literature. Good agreement was obtained between the calculated results and the experimental data.

2. The SMAW, SMAW+SR, SMAW+SR+LTS, LSM, and LSM+LTS processes for repairing of overlaying of Inconel 182 were also simulated. The Cr depletion profile was evaluated by the depletion area below the critical Cr concentration (12 mass%). The sample after SR treatment showed the maximum Cr depletion area and subsequent LTS treatment with recovery of IGC/IGSCC resistance showed a slightly smaller Cr depletion area. The sample after LTS treatment following LSM showed a smaller Cr depletion area, and the sample after the LSM process showed the smallest Cr depletion area. These results are in good agreement with the IGC/IGSCC susceptibilities evaluated by the Streicher test, which implies that the current model could be used as an effective tool to predict Cr depletion as well as the corresponding IGC/IGSCC susceptibility of Inconel 182 for different heat treatment conditions.

Acknowledgements

We gratefully acknowledge associate professor Makoto Yoshida, Department of Science

and Engineering, Waseda University, for his help with TEM observations, and Yoichi Mahara and Hiroshi Watanabe, Babcock-Hitachi K.K for their help with the corrosion test.

References

[1] A. McMinn, R. A. Page, Corrosion 44 (4) (1988) 239-247.

[2] R. A. Page, Corrosion 41 (6) (1985) 338-344.

[3] C. L. Briant, E. L. Hall, Corrosion 43 (7) (1987) 437-440.

[4] C. L. Briant, E. L. Hall, Corrosion 43 (9) (1987) 539-548.

[5] N. Saito, S. Tanaka, H. Sakamoto, Corrosion 59 (12) (2003) 1064-1074.

[6] W. T. Tsai, C. L. Yu, J. I. Lee, Scripta Mater. 53 (2005) 505-509.

[7] G. Bao, K. Shinozaki, S. Iguro, M. Inkyo, Y. Mahara, H. Watanabe, Sci. Technol. Weld. Join. 10 (6) (2005) 706-716.

[8] G. Bao, S. Iguro, M. Inkyo, K. Shinozaki, M. Yamamoto, Y. Mahara, H. Watanabe, Weld. World 49 (7/8) (2005) 37-44.

[9] G. Bao, K. Shinozaki, S. Iguro, M. Inkyo, M. Yamamoto, Y. Mahara, H. Watanabe, J. Mater. Process. Technol. 173 (3) (2006) 330-336.

[10] M. Sireesha, S. K. Albert, S. Sundaresan, Metal. Mater. Trans. A 36A (2005) 1495-1506.

[11] D. B. Williams, C. B. Carter, Transmission Electron Microscopy, Plenum Press, 1996.

[12] G. Bao, K. Shinozaki, M. Inkyo, T. Miyoshi, M. Yamamoto, Y. Mahara, H. Watanabe, J. Alloys Compd. 419 (1-2) (2006) 118-125.

[13] H. Cerjak, N. Enzinger, E. Kozeschnik, I. Holzer, Y. Ghanimi, R. Vallant, S. Baumgartner, P. Mayr, Inter-University Research Seminar, Beijing, China, 2005, 37-58.

[14] W. C. Liu, F. R. Xiao, M. Yao, Scripta Mater. 37 (1) (1997) 59-64.

[15] A. Tsuruta: Welding Theory and Design, Tokyo Denki University Press, 1968 (In Japanese).

[16] K. Nishimoto, H. Mori, Y. Nakao, Q. J. Jpn. Weld. Soc. 14 (4) 703-708.

Figure captions:

Fig. 1 Thermal cycle flow of repairing procedure of Inconel 182

Fig. 2 Optical microstructure of Inconel 182 before and after LSM process: (a) SMAW+SR+LTS; (b) LSM

Fig. 3 SEM micrographs of Inconel 182 showing various intergranular microconstituent distributions: (a) SMAW; (b) SMAW+SR; (c) SMAW+SR+LTS; (d) LSM; (e) LSM+LTS

Fig. 4 TEM micrographs of tiny $M_{23}C_6$ from specimen of SMAW+SR+LTS: (a) Bright field TEM image; (b) Dark field TEM image; (c) SADP; (d) Key diagram

Fig. 5 Interdendritic NbC after SMAW procedure

Fig. 6 TEM micrographs of NbC from specimen of SMAW+SR+LTS: (a), (b) Bright field TEM image; (c) SADP; (d) Key diagram

Fig. 7 Comparison of experimental data for Cr depletion [5] and the current model for Inconel 182

Fig. 8 Cr depletion profiles of Inconel 182 for heat treatment and LSM process

Fig. 9 Evaluation Cr depletion zone around the Cr carbide

Fig. 10 Relationship between Cr depletion area and maximum IGC depth

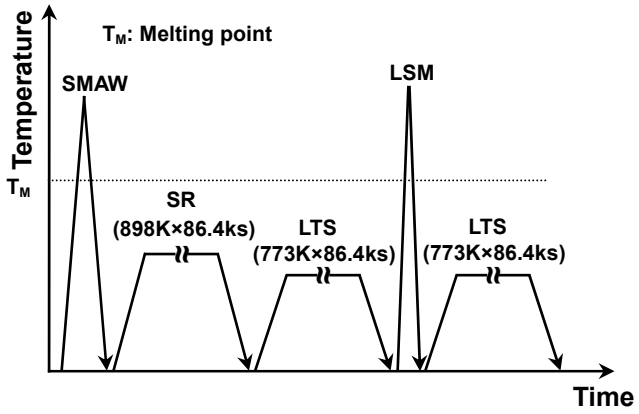
Temperature
T_M: Melting point
SMAW
LSM
T_M
SR
(898K×86.4ks)
LTS
(773K×86.4ks)
LTS
(773K×86.4ks)
Time

Fig. 1

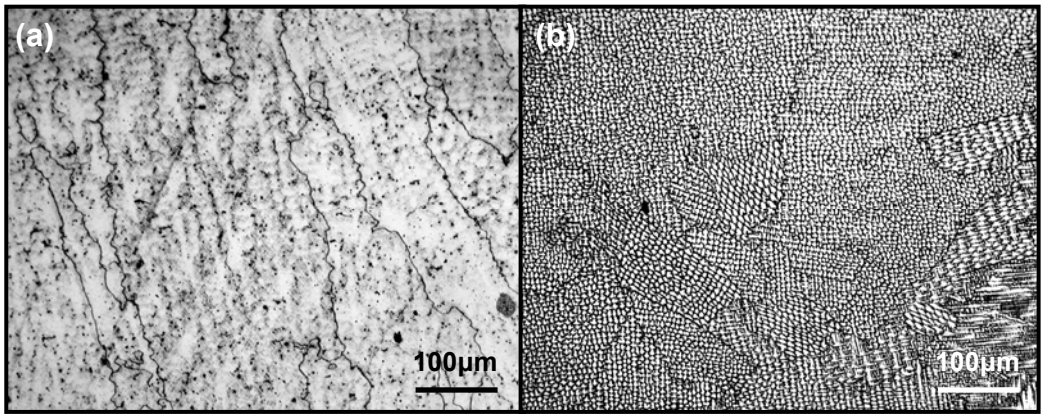

Fig. 2

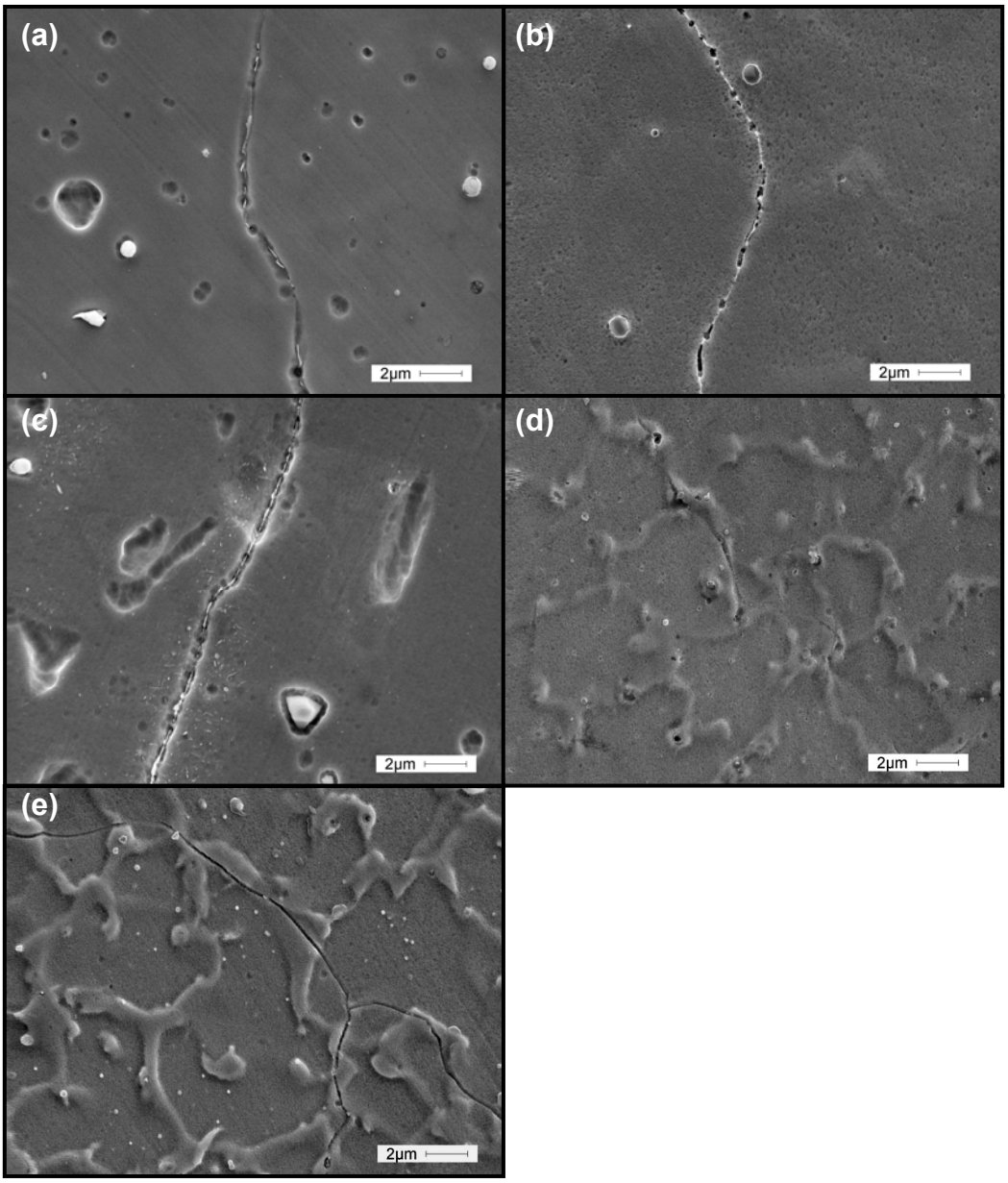

Fig. 3

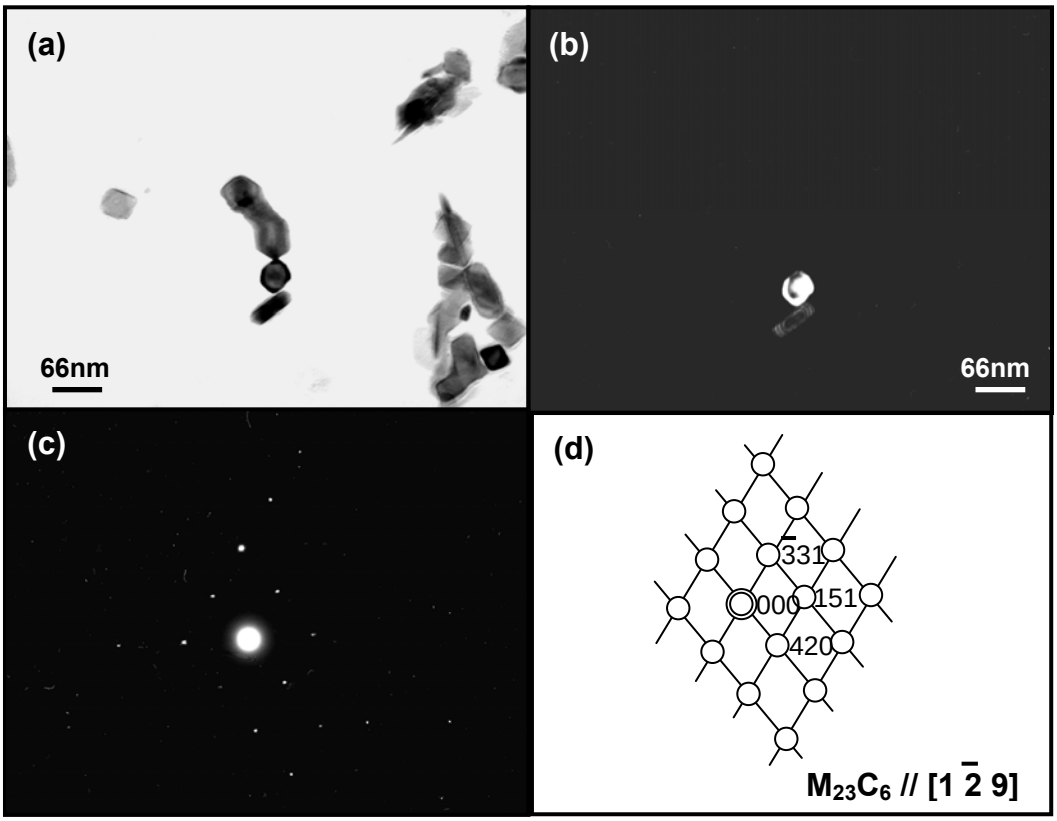

Fig. 4

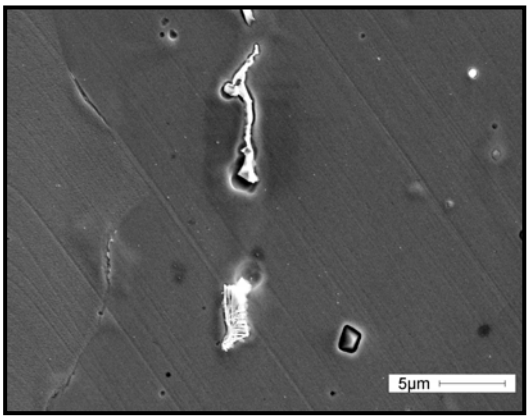

Fig. 5

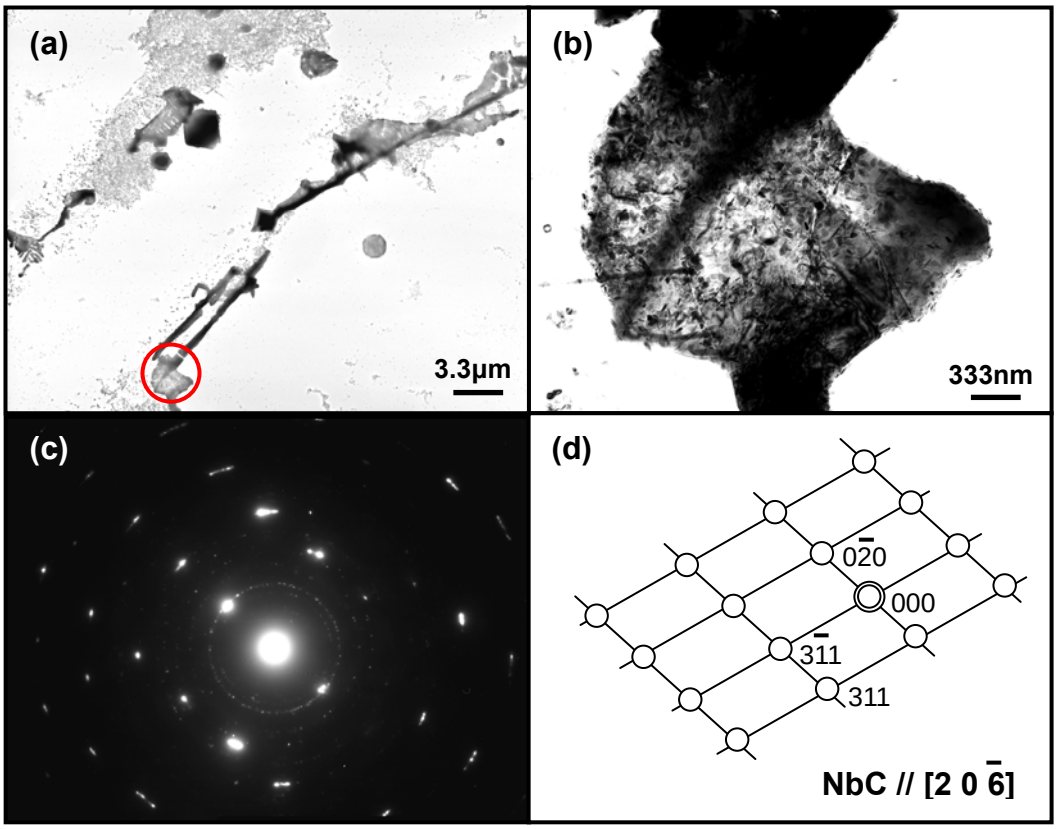

Fig. 6

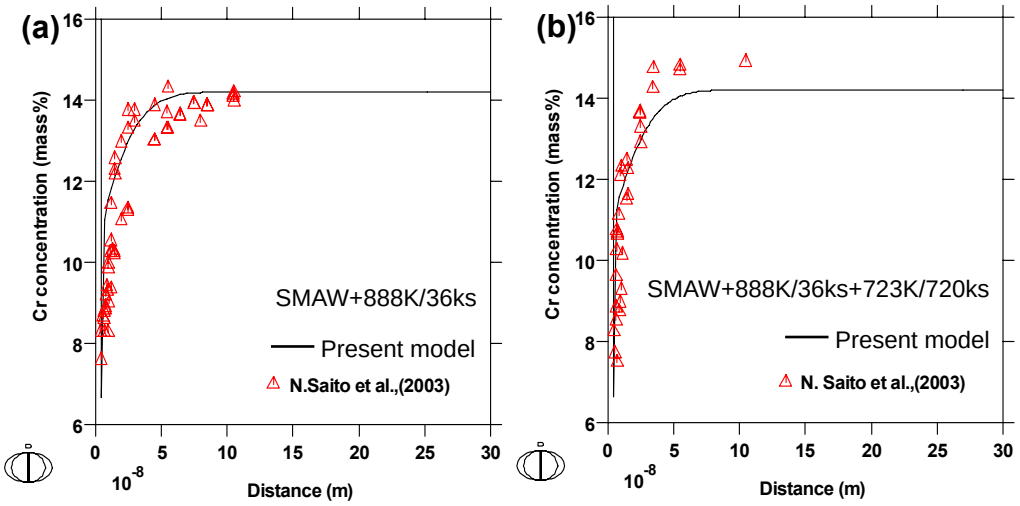
(a)
Cr concentration (mass%)
16
14
12
10
8
6
0
5
10
15
20
25
30
10-8
Distance (m)
SMAW+888K/36ks
Present model
N.Saito et al.,(2003)
(b)
Cr concentration (mass%)
SMAW+888K/36ks+723K/720ks
Present model
N. Saito et al.,(2003)
Distance (m)

Fig. 7

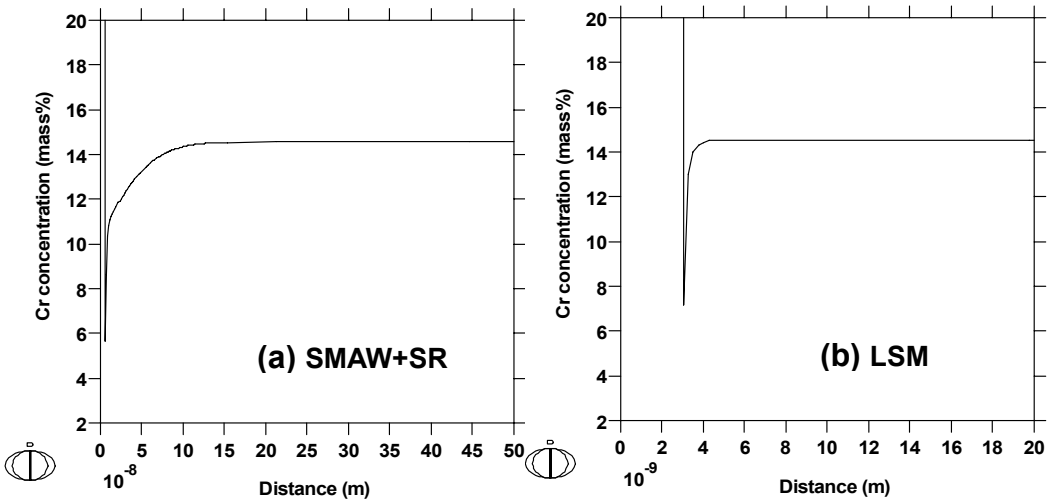
Cr concentration (mass%)
(a) SMAW+SR
10^-8
Distance (m)
Cr concentration (mass%)
(b) LSM
10^-9
Distance (m)

Fig. 8

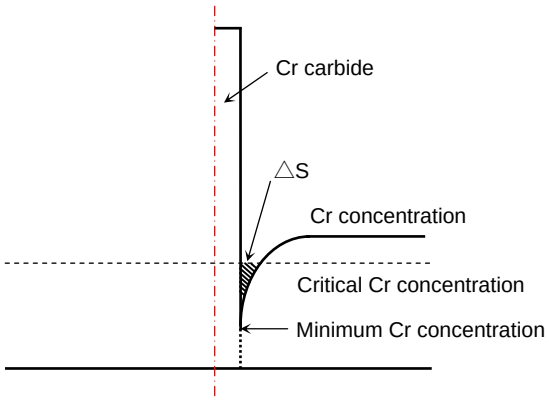
Cr carbide
△S
Cr concentration
Critical Cr concentration
Minimum Cr concentration

Fig. 9

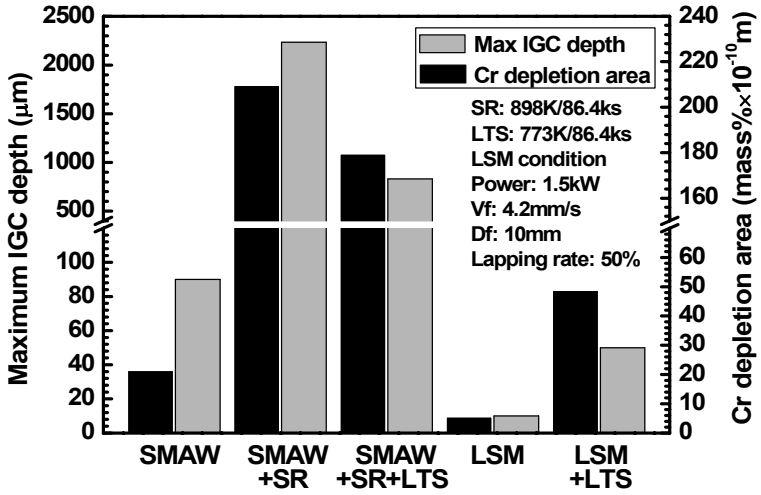
Max IGC depth
Cr depletion area
SR: 898K/86.4ks
LTS: 773K/86.4ks
LSM condition
Power: 1.5kW
Vf: 4.2mm/s
Df: 10mm
Lapping rate: 50%
Maximum IGC depth (μm)
Cr depletion area (mass%×10^-10m)
2500
2000
1500
1000
500
100
80
60
40
20
0
240
220
200
180
160
60
50
40
30
20
10
0
SMAW
SMAW +SR
SMAW +SR+LTS
LSM
LSM +LTS

Fig. 10

Table 1 Chemical compositions of Inconel 182 used (mass %)

C	Si	Mn	P	S	Cu	Ni	Cr	Fe	Nb+Ta
0.04	0.21	2.76	0.003	0.003	0.03	bal.	14.54	8.66	1.92

Table 2 Conditions of laser surface melting

Laser power (kW)		1.5
Traveling speed (mm/s)		4.2
Defocus length (mm)		10
Lapping rate (%)		50
Ar shielding gas	Coaxial	0.5
($10^{-3}m^3/s$)	Side	0.3
Angle of irradiation (°)		10

Table 3 Calculated NbC amount after SMAW process

	Nb+Ti (mass %)	NbC (volume %)	NbC (at %)
Inconel 182 used	1.92	0.24	0.12
Inconel 182 [5]	1.94	0.24	0.12

Table 4 Constants used for SMAW process

T_0	298K
k	14.9W/m.k
v	1.667mm/s
η	0.8
E	24V
I	170A

Table 5 Calculated initial composition of carbide and matrix at 1015K (mass %) [5]

Component	Matrix	$M_{23}C_6$
Ni	Bal.	-
Cr	14.20	81.95
Fe	7.63	2.03×10^{-2}
C	2.24×10^{-2}	Bal.